

On the magnetic anisotropy and nuclear relaxivity effects of Co and Ni doping in iron oxide nanoparticles

T. Orlando, M. Albino, F. Orsini, C. Innocenti, M. Basini, P. Arosio, C. Sangregorio, M. Corti, and A. Lascialfari

Citation: *Journal of Applied Physics* **119**, 134301 (2016); doi: 10.1063/1.4945026

View online: <http://dx.doi.org/10.1063/1.4945026>

View Table of Contents: <http://scitation.aip.org/content/aip/journal/jap/119/13?ver=pdfcov>

Published by the [AIP Publishing](#)

Articles you may be interested in

[Dense and half-dense NiZnCo ferrite ceramics: Their respective relevance for antenna downsizing, according to their dielectric and magnetic properties at microwave frequencies](#)

J. Appl. Phys. **117**, 084904 (2015); 10.1063/1.4913700

[Effect of the Zn content in the magnetic properties of Co_{1-x}Zn_xFe₂O₄ mixed ferrites](#)

J. Appl. Phys. **113**, 17B513 (2013); 10.1063/1.4796173

[Origin of magnetic anisotropy in ZnO/CoFe₂O₄ and CoO/CoFe₂O₄ core/shell nanoparticle systems](#)

Appl. Phys. Lett. **101**, 252405 (2012); 10.1063/1.4771993

[High temperature magnetic properties of Co_{1-x}Mg_xFe₂O₄ nanoparticles prepared by forced hydrolysis method](#)

J. Appl. Phys. **111**, 07B530 (2012); 10.1063/1.3677923

[The temperature dependence of magnetic properties for cobalt ferrite nanoparticles by the hydrothermal method](#)

J. Appl. Phys. **108**, 084312 (2010); 10.1063/1.3499289



NEW Special Topic Sections

NOW ONLINE
Lithium Niobate Properties and Applications:
Reviews of Emerging Trends

AIP | Applied Physics Reviews

On the magnetic anisotropy and nuclear relaxivity effects of Co and Ni doping in iron oxide nanoparticles

T. Orlando,^{1,2,a)} M. Albino,³ F. Orsini,⁴ C. Innocenti,³ M. Basini,^{4,5} P. Arosio,⁴ C. Sangregorio,^{3,6} M. Corti,¹ and A. Lascialfari^{4,5}

¹Department of Physics, Università di Pavia, and Consorzio INSTM, Pavia 27100, Italy

²Research Group EPR Spectroscopy, Max Planck Institute for Biophysical Chemistry, Göttingen 37077, Germany

³Department of Chemistry "Ugo Schiff," Università di Firenze, and Consorzio INSTM, Sesto Fiorentino 50019, Italy

⁴Department of Physics, Università degli Studi di Milano, and Consorzio INSTM, Milano 20133, Italy

⁵CNR-S3, Istituto di Nanoscienze, Modena 41125, Italy

⁶CNR-ICCOM and Consorzio INSTM, Sesto Fiorentino 50019, Italy

(Received 30 October 2015; accepted 19 March 2016; published online 1 April 2016)

We report a systematic experimental study of the evolution of the magnetic and relaxometric properties as a function of metal (Co, Ni) doping in iron oxide nanoparticles. A set of five samples, having the same size and ranging from stoichiometric cobalt ferrite (CoFe_2O_4) to stoichiometric nickel ferrite (NiFe_2O_4) with intermediate doping steps, was *ad hoc* synthesized. Using both DC and AC susceptibility measurements, the evolution of the magnetic anisotropy depending on the doping is qualitatively discussed. In particular, we observed that the height of the magnetic anisotropy barrier is directly proportional to the amount of Co, while the Ni has an opposite effect. By Nuclear Magnetic Resonance Dispersion (NMR-D) experiments, the experimental longitudinal r_1 and transverse r_2 relaxivity profiles were obtained, and the heuristic theory of Roch *et al.* was used to analyze the data of both r_1 and, for the first time, r_2 . While the experimental and fitting results obtained from r_1 profiles were satisfying and confirmed the anisotropy trend, the model applied to r_2 hardly explains the experimental findings. © 2016 AIP Publishing LLC. [<http://dx.doi.org/10.1063/1.4945026>]

I. INTRODUCTION

Magnetic nanostructured materials usually display physical properties that are significantly different from the ones of the bulk. In ferro- or ferrimagnetic nanoparticles (NPs), the multi-domain spin arrangement typical of the bulk ferromagnets is absent, and the energy equilibrium configuration favours a single magnetic domain. As a consequence, the spins inside each NP are aligned along a particular direction and give rise to a large magnetic moment, which can be thought as a "superspin."

Their basic properties have been studied both theoretically and experimentally since the 1950s^{1,2} but, in the last two decades, the evolution of the synthesis techniques allowed obtaining excellent quality monodispersed samples, having a well-defined size and shape. This allowed to explore and understand the physical phenomena at the nanoscale.³ At the same time, the possibility to coat the magnetic nanoparticles with different kind of organic materials opens the possibility to use them in several state-of-the-art biomedical and technological applications.

Among the magnetic materials, iron oxides, such as magnetite (Fe_3O_4) or maghemite ($\gamma\text{-Fe}_2\text{O}_3$), are generally used as magnetic core, being the only ones which have been already approved by U.S. Food and Drug Administration (FDA) and European Medicines Agency (EMA).⁴ These systems can help in various aspects of clinical practice,^{5,6} working as

contrast agents in magnetic resonance imaging (MRI),^{7,8} drug carriers in magnetic transport,⁹ or therapeutic agents in magnetic fluid hyperthermia (MFH).¹⁰ Furthermore, new perspectives are opening in the field of the multifunctional magnetic nanostructures, which can be used simultaneously for different tasks.

Nevertheless, even if novel synthesized nanostructures are able to successfully accomplish one or two tasks, a real multifunctional object has not been completely realized yet. Consequently, the research of new materials whose properties can be properly tailored is of great interest. To this aim, the possibility to dope the iron oxide magnetic core with transition metal ions, obtaining optimized magnetic properties, can boost the use of nanoparticles for such applications.^{11,12} In particular, a greater magnetization can improve the performance in magnetic transport, a high transverse nuclear relaxation rate brings to a better image contrast, while the kind of magnetic ion, the coating, and particularly the size are critical parameters for all applications.

The doping of the ferrite magnetic core with high anisotropy metal ions can be a feasible strategy. Several iron oxide nanostructures doped with cobalt, zinc, or gadolinium have been already synthesized and investigated,^{13–17} but a complete and systematic study on the effect of Co and Ni doping on the magnetic properties is still missing. In order to address this issue, five cobalt and nickel substituted ferrite ($\text{Co}_x\text{Ni}_y\text{Fe}_{3-x-y}\text{O}_4$) nanoparticles with fixed size were synthesized, using a step-by-step doping, from stoichiometric Co-ferrite to stoichiometric Ni-ferrite.

^{a)}Electronic mail: tomas.orlando@mpibpc.mpg.de

In the first part of the work, DC and AC susceptibility measurements were performed, allowing us to determine both static and dynamic properties. The magnetic anisotropy, the blocking temperature, and the main parameters governing the magnetization reversal (like, e.g., the attempt time τ_0 and the energy barrier E_b) were explored upon the doping level. Some literature data about undoped iron oxide nanoparticles were also taken into account and used as reference.

The second part of the work reports NMR relaxometry data. In particular, the complete relaxivity profiles were acquired for both longitudinal (r_1) and transverse (r_2) directions over a wide range of frequencies (10 kHz–255 MHz and 10 kHz–60 MHz, respectively). The heuristic theoretical model proposed some years ago by Roch *et al.* in Ref. 18 was tested for r_1 and, for the first time, for r_2 .

II. SYNTHESIS AND EXPERIMENTAL TECHNIQUES

The samples were synthesized by thermal decomposition of the metallo-organic precursors in non-coordinating high boiling solvents with surfactant. A mixture of Fe(acac)₃, Co(acac)₂·H₂O, Ni(acac)₂, oleylamine, and oleic acid in benzyl ether was stirred for 15 min under nitrogen flux at room temperature, then heated up to 290 °C, and refluxed for 15 min. After the cooling down till room temperature, ethanol was added, in order to allow precipitation. The solid precipitate was isolated with a magnet and washed several times using ethanol. The obtained NPs were coated with oleic acid. In order to disperse the NPs in water, the oleic acid of the coating was substituted with the polyacrylic acid (PAA), which is hydrophylic and provides biocompatibility. Different amounts of cobalt and nickel were used in order to obtain a set of five samples of intermediate composition Co_xNi_yFe_{2-x-y}O₄, ranging from stoichiometric CoFe₂O₄ to stoichiometric NiFe₂O₄. In the following, the samples are labeled as CoXNiY, where X and Y denote the approximation to the first decimal digit of the Co and Ni content x and y , respectively (Table I). The other synthesis parameters were adjusted in order to fix the size of the nanostructures NPs to the same value (ca. 7 nm) for all the samples.

Average diameter and size distribution of NPs were evaluated by Transmission Electron Microscopy (TEM), using a CM12 Philips microscope operating at 100 kV. The samples were prepared by drop drying a diluted suspension of NPs in hexane onto 200 mesh carbon-coated copper grids. The recorded images were analyzed with the ImagePro-Plus

TABLE I. Chemical composition and size analysis of the Co-Ni-ferrites. d_{TEM} ($d_{mean} \pm \delta d$) is the size obtained by fitting the diameter histograms from TEM images with Eq. (1). The last two columns report the height (h_{AFM}) and the width (w_{AFM}) of the particles obtained from AFM images.

Sample	Composition	d_{TEM} (nm)	h_{AFM} (nm)	w_{AFM} (nm)
Co8Ni0	Co _{0.82} Fe _{2.18} O ₄	7.4 ± 1.5	9.1 ± 1.2	12.6 ± 1.2
Co6Ni3	Co _{0.63} Ni _{0.32} Fe _{2.05} O ₄	7.0 ± 1.1	9.2 ± 1.2	12.6 ± 1.2
Co4Ni6	Co _{0.42} Ni _{0.56} Fe _{2.02} O ₄	6.6 ± 1.0	9.8 ± 1.3	13.1 ± 1.4
Co2Ni8	Co _{0.17} Ni _{0.85} Fe _{1.98} O ₄	7.0 ± 1.3	10.0 ± 1.3	14.4 ± 1.5
Co0Ni10	Ni _{1.02} Fe _{1.96} O ₄	7.3 ± 1.9	9.6 ± 1.2	12.6 ± 1.2

software. The statistical analysis was carried out over 400–600 NPs.

AFM imaging was performed using a Bruker Nanoscope Multimode IIIId system operating in air in tapping-mode. AFM images were collected using the RMS amplitude of the cantilever as the feedback signal for the vertical sample position. The RMS free amplitude of the cantilever was approximately 15 nm and the relative set-point above 95% of the free amplitude. Rectangular silicon probes with nominal spring constant around 2.5 N/m (NSG01, NT-MDT) and cantilever length of 120 μm were used. The cantilever resonance frequency was about 130 kHz.

DC and AC susceptibility measurements were performed by a MPMS-XL7 Quantum Design Superconducting Quantum Interference Device (SQUID) magnetometer, operating in the temperature range 2–300 K and in the field range 0–5 T. Zero-field cooled (ZFC), field-cooled (FC), and hysteresis curves were acquired on dried samples at different applied magnetic fields. The frequency-dependence of the sample magnetic response was investigated in the range of frequency 10–10 000 Hz.

The NMR-Dispersion profiles were measured on water suspensions of each sample. Longitudinal and transverse nuclear relaxation times, T_1 and T_2 , respectively, were evaluated over the range 10 kHz–255 MHz (limited to 60 MHz for T_2) for the ¹H (proton) Larmor frequency, corresponding to an applied magnetic field in the range 2.3×10^{-4} –6.0 T. In order to cover such a wide range, three different instruments were used: (1) a Tecmag Apollo spectrometer with an Oxford superconducting magnet for the very high fields' region, i.e., from 60 to 255 MHz; (2) a Stellar Spinmaster with a standard electromagnet for the intermediate range, 10–60 MHz; and (3) a Stellar SMARtracer, working with the Fast-Field Cycling technology, for the low and very low fields' range, corresponding to 10 kHz–10 MHz. In the first two cases, standard pulse sequences were selected, that is, Saturation Recovery for T_1 and Car-Purcell-Meiboom-Gill (CPMG) for T_2 . For the very low field range ($\nu < 4$ MHz for T_1 and $\nu < 3.5$ MHz for T_2), *ad hoc* pre-polarized sequences were used to increase the NMR proton signal.^{19,20}

III. MORPHOLOGICAL CHARACTERIZATION

The morphological characterization was performed using TEM micrographs, a typical example of which is reported in Fig. 1 for Co4Ni6 sample, as representative of the all series. As commonly reported, the diameter (d) histograms extracted from TEM images were fitted to a lognormal law

$$\rho(d) = \frac{1}{d\sqrt{2\pi\sigma^2}} e^{-\frac{[\ln(d)-\mu]^2}{2\sigma^2}}, \quad (1)$$

where μ and σ are the distribution parameters. The mean diameter is $d_{mean} = e^{\mu+\sigma^2/2}$, and its standard deviation is $\delta d = e^{\mu+\sigma^2/2} \sqrt{e^{\sigma^2} - 1}$. As requested, the mean size of prepared Co-Ni-ferrites, which appear spherical shaped, is ~ 7 nm for all the samples (Table I).

The NPs' morphology was also investigated by Tapping Mode Atomic Force Microscopy (TM-AFM), which allowed

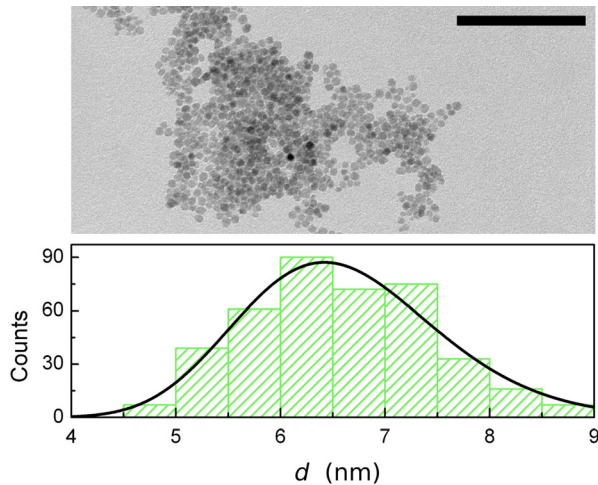


FIG. 1. TEM image of the sample Co₄Ni₆ (scale bar = 100 nm), the corresponding magnetic core diameter histogram (bars), and the best fit curve to a lognormal distribution (line).

the evaluation of the overall size of the NPs, namely, that of the magnetic core plus its PAA coating. Besides the presence of NPs agglomerates of different sizes, AFM can distinguish single NPs, as shown in the topography image of Fig. 2. The analysis of several AFM topography images allowed to estimate the NPs' average size, measuring both the height and the width: Fig. 2 and Table I summarize the results. In particular, the NPs' average height obtained by AFM is greater than the size estimated from TEM data, due to the presence of the PAA coating, which results of the order of 2 nm for all the samples. On the other hand, the particle width is overestimated, possibly due to: (i) the sample-AFM tip convolution effect; (ii) the pressure applied by the AFM tip on the soft NPs' coating during the sample scan and induced by the capillary forces.

In TM-AFM, the sample is scanned by an oscillating cantilever whose oscillation parameters (amplitude and phase) are sensitive to both topography and mechanical properties of the sample surface. In particular, a shift of the phase results from a different visco-elastic interaction between the sample and the AFM tip. Thus, a phase image

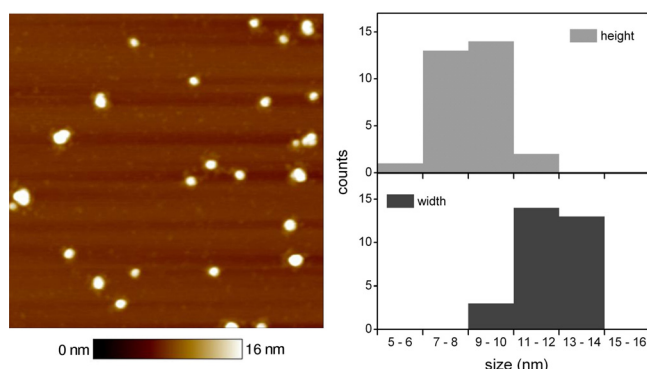


FIG. 2. On the left, the topography of the sample Co₈Ni₀ is shown. Single NPs as well as small NPs clusters are visible (scan area = 500 × 500 nm²). The corresponding AFM histograms of the height and the width of the NPs for the same sample are reported on the right.

obtained by mapping the phase angle shifts across the sample brings information about its mechanical properties. In the case of our NPs, soft (PAA coating) and stiff (magnetic core) regions appear at different image contrast, and information about the whole sample structure can be assessed. As an example in Fig. 3, an AFM topography image and its corresponding AFM phase image of the Co₈Ni₀ sample on a mica support are reported. Even if in this case a reliable quantitative evaluation of the particle size is not possible due to the high pressure applied by the tip, a rough estimation of the coating thickness can be done, resulting in good agreement with the topography data.

IV. DC SUSCEPTIBILITY MEASUREMENTS

Iron oxide nanoparticles are single domain nanoparticles characterized by a high value of the single particle magnetic moment μ_{SP} and by an uniaxial magnetic anisotropy.²¹ Using a first order approximation, the expression of the anisotropy energy is $E_A(\theta) = K_{eff}V \sin^2 \theta$, where K_{eff} is the effective anisotropy constant, V is the particle volume, and θ is the angle between the particle magnetization \mathbf{M} and the anisotropy axis. The two equilibrium positions, corresponding to $\theta = 0$ and $\theta = \pi$, are separated by the energy barrier $E_b = K_{eff}V$. If $k_B T \gtrsim E_b$, the flip of the magnetization between the two minima is allowed (superparamagnetic regime). In case of non-interacting particles, the characteristic relaxation time, known as Néel relaxation time τ_N , is given by an Arrhenius-like expression:^{1,2} $\tau_N = \tau_0 \exp(\frac{E_b}{k_B T})$, where τ_0 is the “attempt time.” The external magnetic field at enough high temperature easily drives the magnetization of an ensemble of single domain nanoparticles, which thus behaves like a paramagnetic system. As a consequence, the M vs. H curves collected at room temperature (300 K) do not show open hysteresis, being $H_C = 0$, as shown in Fig. 4. Furthermore, as can be noticed from the same figure, the saturation magnetization M_S scales up with the Co-doping, being the highest for stoichiometric Co-ferrite ($M_S = 83 \text{ A m}^2/\text{kg}$ for Co₈Ni₀) and the smallest for stoichiometric Ni-ferrite ($M_S = 49 \text{ A m}^2/\text{kg}$ for Co₀Ni₁₀). This is in agreement with the values reported in the literature, both for bulk ferrites^{22,23} and nanoparticles.²⁴

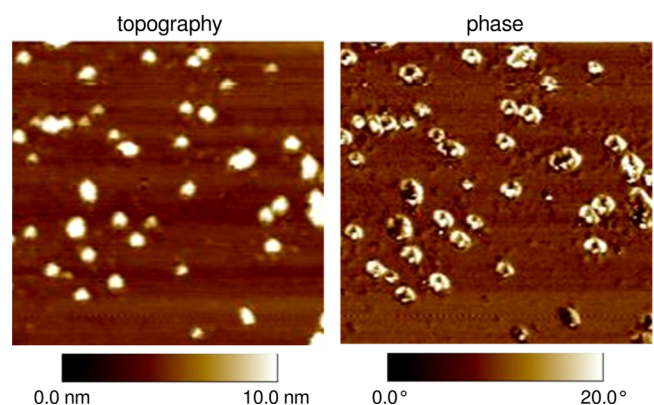
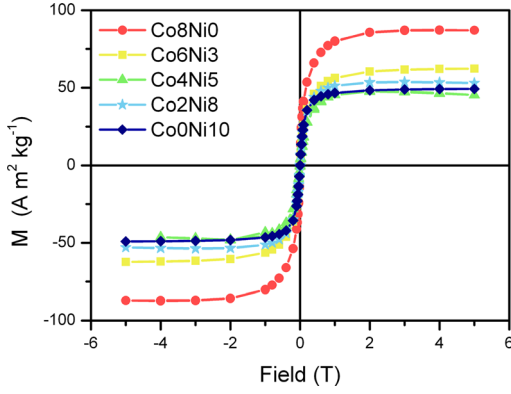


FIG. 3. AFM topography image (left) and corresponding AFM phase image (right), collected simultaneously on the same area, of Co₈Ni₀ on mica support. The phase image allows the visualization of the NPs PAA coating (white rings) as well as the NPs magnetic core (dark circles). The scan area is 300 × 300 nm².

FIG. 4. M vs. H curves at $T = 300$ K.

The fluctuation rate $1/\tau_N$ of the magnetization between the energy minima slows down when the temperature decreases. At a certain temperature T_B , defined as blocking temperature, the Néel relaxation time τ_N becomes comparable to the experimental measuring time τ_m . The separation between superparamagnetic and blocked regimes occurs in correspondence to the blocking temperature T_B , which in the region of validity of the Arrhenius law is given by $T_B = E_b/(k_B \ln(\tau_m/\tau_0))$.

For an ensemble of single domain NPs, a distinctive peak is expected in the ZFC curve when $T = T_{MAX}$,²⁶ while the FC one should increase monotonously when the temperature decreases. Assuming the simple relation $E_b \propto V$, taking into account an ensemble of non-interacting nanoparticles and their lognormal size distribution, as a first approximation a lognormal distribution $\rho(E_b)$ can be associated to the

energy barrier as well, i.e., $\rho(E_b) = \frac{1}{E_b \sqrt{2\pi\sigma_E^2}} e^{-\frac{(\ln E_b - \mu_E)^2}{2\sigma_E^2}}$. The

width of the ZFC peak is directly related to $\rho(E_b)$. In particular, using the formula described in Refs. 27 and 28, the magnetization can be written as

$$M_{ZFC} = \frac{\mu_0 H M_S^2}{3K_{eff}^2} \left(\frac{1}{k_B T} \int_0^{E_{lim}} E_b^2 \rho(E_b) dE_b + \int_{E_{lim}}^{\infty} E_b \rho(E_b) dE_b \right), \quad (2)$$

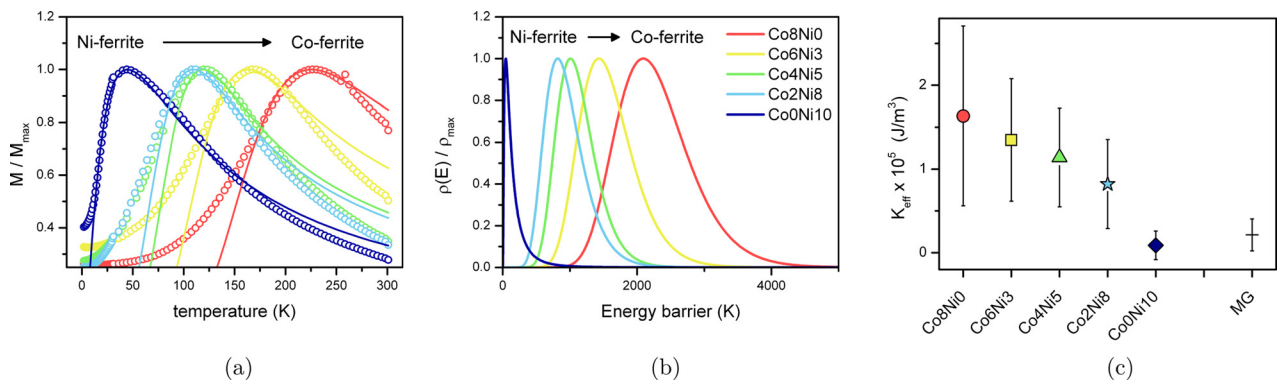


FIG. 5. (a) ZFC curves (circles) collected at 50 Oe and normalized with respect to the maximum. The continuous line is the best fit curve to Eq. (2) in a temperature range of 100 K around the maximum of M . (b) The obtained log-normal energy barrier distributions, whose mean (E_{mean}) and standard deviations (δE) are reported in Table II. (c) K_{eff} evaluated using the approximated relation $K_{eff} = E_b/V_{mean}$, where $E_b = E_{mean}$ and V_{mean} is the average particle volume. The error bars represent the absolute error obtained taking into account the standard deviation of both the energy barrier distribution and the volume distribution. The results are plotted as a function of the doping. An undoped iron oxide sample of comparable size and labeled MG²⁵ was also considered.

where the first integral represents the contribution of unblocked particles, while the second integral corresponds to that of the blocked ones. Beside the assumption of uniaxial anisotropy, the previous model holds for low applied magnetic fields, i.e., when the linear response is still valid, and for non-interacting particles. The first condition can be satisfied by taking into account very low field magnetization measurements, i.e., the ZFC curves collected at $H = 50$ Oe. On the contrary, the interparticle interactions are not completely negligible in the experimental practice, especially for powder samples. However, the problem of the interaction among NPs is still a matter of debate in the literature, and no universal model has been formulated, although some papers report good agreement between the experimental data and the theory.^{29–39} For this reason, we will keep the present discussion at the simpler level of non-interacting NPs, having well in mind that the conclusions that will be traced regarding the estimated values of the main physical quantities (E_b , K_{eff} , τ_0 , etc.) remain a mean to give their qualitative trends as a function of doping.

The ZFC data are presented in Fig. 5(a). At a first glance, the behaviour of the T_{MAX} as a function of the doping is clear: starting from Co0Ni10, which displays $T_{MAX} = 44$ K, the progressive doping with cobalt produces a continuous increase of the peak temperature position, till Co8Ni0, for which $T_{MAX} = 226$ K. From now on, for the reasons outlined above, we will identify T_{MAX} with T_B , the “blocking temperature” revealed by the ZFC magnetization curve maximum, where $1/\tau_N \sim 1/\tau_m^{ZFC}$ occurs, being $1/\tau_m^{ZFC} \sim 2\pi \cdot 0.1$ Hz the typical measuring time of a SQUID magnetometer in DC mode.

To extract the general trend of E_b , K_{eff} , and τ_0 as a function of doping, the ZFC curve in the peak region was fitted using Eq. (2), assuming a log-normal distribution for energy barriers. The best fit curves are shown as continuous lines in Fig. 5(a), while the best parameters are reported in Table II. The fitting procedure was applied in the temperature region strictly around the peak, whose position and width are satisfactorily reproduced. The fitting is not accurate on the queues of the distribution, a discrepancy mainly due to the limited validity of the model, which does not take into

TABLE II. Blocking temperature at 50 Oe, the mean energy E_{mean} and its standard deviation δE obtained by the fit of ZFC at 50 Oe with Eq. (2), and the effective anisotropy constant K_{eff} .

Sample	M_S (A m ² /kg)	T_B^{50Oe} (K)	E_{mean} (K)	δE (K)	K_{eff} (J/m ³)
Co8Ni0	87	226	2510	623	1.63×10^5
Co6Ni3	62	165	1748	467	1.35×10^5
Co4Ni6	47	120	1238	308	1.14×10^5
Co2Ni8	54	109	1065	352	8.21×10^5
Co0Ni10	49	44	131	230	8.90×10^3

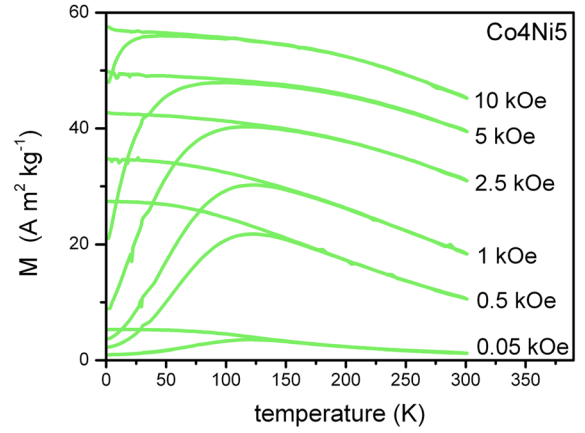
account, e.g., the interactions between the particles. From this simplified model, it was possible to obtain an approximate estimation of the energy barrier (mean and width of the distribution). In Fig. 5(b), the log-normal distributions of the energy barriers calculated using the best-fit parameters extracted from ZFC curves (Table II) are shown.

To compare different kind of samples and to highlight more clearly the influence of the doping on the anisotropy barrier, the effective anisotropy constant K_{eff} was evaluated using the relation $K_{eff} = E_b/V_{mean}$, where $E_b = E_{mean}$, and V_{mean} is the volume calculated using the mean size estimated by TEM images analysis and considering a spherical shape. The results are shown in Fig. 5(c). A maghemite sample of comparable size was also considered,²⁵ as reference compound characterizing the undoped behaviour. As expected, cobalt doped NPs exhibit a magnetic anisotropy higher than the one of the undoped iron oxide particles. Furthermore, a clear trend is easy to identify: the greater is the amount of Co doping, the higher is the effective anisotropy constant.⁴⁰ On the contrary, Ni doping seems to produce the opposite effect, since K_{eff} of Co0Ni10 is lower than that of undoped iron oxide NPs.

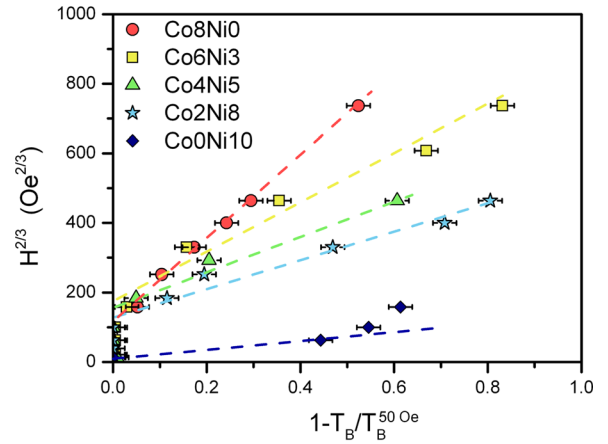
When an external magnetic field is applied, the energy barrier is reduced.⁴¹ As a consequence, the blocking temperature moves to lower values and eventually disappears for high fields. This trend of T_B as a function of H can be easily recognized in Fig. 6(a), where the ZFC/FC curves collected at different magnetic fields are reported for Co4Ni6 as typical example. The relation between T_B and H can be approximately described by a power law

$$H^{2/3} \sim \left(1 - \frac{T_B}{T_B^{50Oe}}\right), \quad (3)$$

where T_B^{50Oe} is the blocking temperature at the lowest applied field.⁴² This relation, known as the Almeida-Thouless law, originally foreseen for describing spin glass behaviour, can hold true also for superparamagnetic systems,^{43,44} under the assumption $\mu_{SP} \cdot H \ll E_b$. A deviation from Almeida-Thouless regime can thus occur when the energy associated to the magnetic field is comparable to or higher than the anisotropy energy barrier, i.e., $\mu_{SP} \cdot H \geq E_b$. In Fig. 6(b), Eq. (3) is represented in the usual linear form, plotting $H^{2/3}$ as a function of $\left(1 - \frac{T_B}{T_B^{50Oe}}\right)$ for all the samples. The slope of the line is proportional to the height of the anisotropy barrier. All the samples containing cobalt show no deviation from



(a)



(b)

FIG. 6. (a) ZFC/FC curves collected at different external magnetic fields for Co4Ni6, shown as representative of the behavior of all samples. (b) The blocking temperatures T_B obtained at different fields H reported as $H^{2/3}$ vs $(1 - T_B/T_B^{50Oe})$. The dashed lines are guides for eyes.

linearity, and for weak fields (≤ 1000 Oe), the blocking temperature is constant, being the anisotropy barrier so high that it is not affected by the field. On the other hand, the stoichiometric Ni-ferrite (Co0Ni10), having a lower anisotropy barrier, shows a different behaviour, and the onset of a non-linear regime is observed for $H^{2/3} \sim 62$ Oe^{2/3} (i.e., $H_T \sim 500$ Oe).

V. AC SUSCEPTIBILITY MEASUREMENTS

The spin dynamics of the systems can be described by the two susceptibility components observed when an alternating magnetic field is applied: an in-phase, or real, component χ' , and an out-of-phase, or imaginary, component χ'' . The latter indicates dissipative processes and, in case of superparamagnetic systems, displays a peak at the so-called blocking temperature $T_B^{AC}(\nu)$, occurring when the measuring (of the applied alternating field) frequency $\omega_{AC} = 2\pi\nu_{AC}$ matches a typical correlation frequency of the system $1/\tau_c$ (e.g., the Néel reversal frequency), such that $\omega_{AC} \cdot \tau_c \sim 1$.

In Fig. 7(a), the evolution upon temperature of the AC susceptibility components acquired at log-spaced frequency intervals in the range 10–10 000 Hz is reported for Co2Ni8,

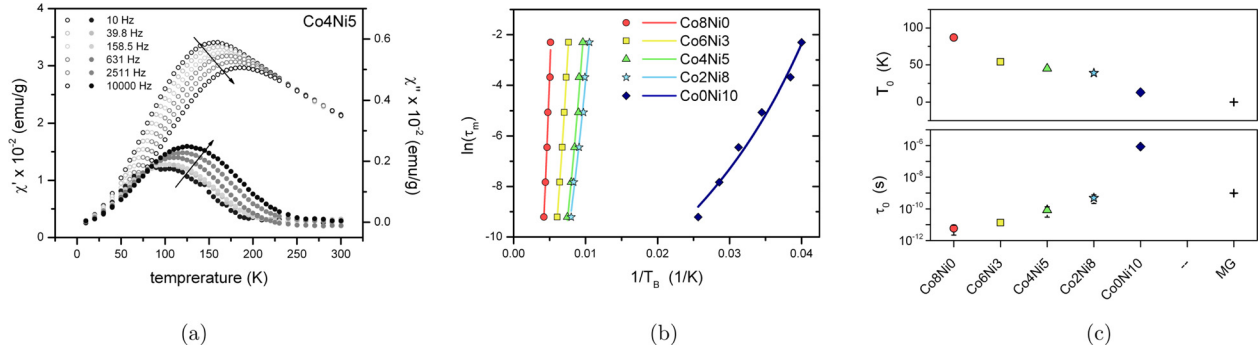


FIG. 7. (a) The in-phase χ' (open circles) and the out-of-phase χ'' (solid circles) AC susceptibility components are reported for different frequencies of the alternating magnetic field (ν_{AC}) for Co4Ni6 sample. The arrows indicate the increasing frequencies. (b) The blocking temperatures obtained from χ'' curves fitted using the Vogel-Fulcher model (Eq. (4)), represented as a continuous line, in the form: $\ln(\tau_m) = \ln(\tau_0) + E_b/(T - T_0)$. (c) Doping dependence of T_0 and τ_0 estimated from AC susceptibility measurements. Data obtained on the undoped compound (MG from Ref. 25) are also shown as reference.

as representative example. Collecting $T_B^{AC}(\nu)$, the dynamics of the system can be investigated by means of the Arrhenius law (non interacting NPs) or the phenomenological Vogel-Fulcher (VF) model, which includes a heuristic correction for interparticle interactions introducing in the relaxation time expression a phenomenological parameter T_0 as follows:

$$\tau_N = \tau_0 \exp\left(\frac{E_b^{AC}}{T - T_0}\right). \quad (4)$$

The results of the fitting procedure are shown in Fig. 7(b), while the values of the best-fit parameters τ_0 and T_0 are reported in Table III and, graphically, in Fig. 7(c). In order to avoid high errors on the fit parameters (in principle three of them are free in Eq. (4)) due to the small range of frequencies explored by the technique, the energy barrier E_b^{AC} has been fixed equal to the value E_{mean} estimated by DC susceptibility measurements (Table II).

The behaviour of the phenomenological parameter T_0 as a function of cobalt doping is related to the dipolar interparticle interactions E_{d-d} , the energy of which depends on the single particle magnetic moment μ_{SP} and on the interparticle distance D as $E_{d-d} \sim \mu_{SP}^2/D^3$. Assuming that the distance is of the same order of magnitude for all the samples, as it depends mainly on the coating, the T_0 value is driven by the magnetic moment of the particle. The T_0 behaviour as a function of the doping level is consistent with the one observed for M_S . The obtained attempt time τ_0 is within the range 10^{-12} – 10^{-9} s, typical for superparamagnetic particles. The shortening of τ_0 with increasing the Co content can be qualitatively ascribed to the increased interparticle interactions.^{46,47}

TABLE III. Parameters of the Vogel-Fulcher model (Eq. (4)), i.e., attempt time τ_0 and threshold temperature T_0 .

Sample	τ_0 (s)	T_0 (K)
Co8Ni0	$5.8(3.6) \times 10^{-12}$	87(4)
Co6Ni3	$1.4(0.3) \times 10^{-11}$	54(1)
Co4Ni6	$8.3(5.3) \times 10^{-11}$	45(5)
Co2Ni8	$4.9(2.7) \times 10^{-10}$	39(2)
Co0Ni10	$8.7(2.8) \times 10^{-7}$	13(1)

VI. NMR RELAXOMETRY

$^1\text{H-NMR}$ measurements were performed on water dispersions of nanoparticles having the PAA as stabilizing coating. The nuclear longitudinal (r_1) and transverse (r_2) relaxivities were evaluated

$$r_i = \frac{(1/T_i)_{meas} - (1/T_i)_{matrix}}{C}; \quad i = 1, 2, \quad (5)$$

where $T_{i,meas}$ is the measured nuclear relaxation time of the sample, while $T_{i,matrix}$ is the nuclear relaxation time of the diamagnetic matrix (water in this case) without the magnetic nanoparticles dispersed in; C is the magnetic ion concentration: for the measured samples, C was in the range 0.5–1.5 mM. The usual units for the relaxivities are $\text{s}^{-1} \text{mM}^{-1}$.

The longitudinal (r_1) and transverse (r_2) relaxivities for all the investigated samples are shown in Figs. 8(a) and 8(b), respectively. The longitudinal relaxivity follows the typical behaviour of superparamagnetic nanoparticles, where one can distinguish: (i) a low frequencies plateau, due to the contribution of the Néel relaxation, related to the anisotropy energy; (ii) a maximum at intermediate frequencies whose position is strictly related to the size of the nanoparticle:⁸ in our case, the maxima of the r_1 curves fall around 6 MHz, reflecting the fact that all the samples have the same core size within few tenths of nanometer ($d \sim 7$ nm); and (iii) a rapid decrease at high frequencies as a consequence of the so-called Curie relaxation, where the contribution of the proton diffusion correlation time τ_D relative to the nanoparticles dominates. A scaling of the r_1 values with the doping is observed over the whole frequency range. In particular, the stoichiometric Co-ferrite (Co8Ni0) has the highest r_1 , and the stoichiometric Ni-ferrite (Co0Ni10) has the lowest, while the other samples have intermediate values, according with the doping percentage. This is mainly a consequence of the magnetic moment of the particles, being the relaxation rate proportional to the single particle magnetic moment,¹⁸ as detailed in Sec. VII.

Furthermore, the effect of doping can be pointed out by looking at the evolution of the shape of the low field part of the curve. In particular, the stoichiometric Ni-ferrite (Co0Ni10) is characterized by a marked maximum and a smoothed low field dispersion (the dip between 0.1 MHz and

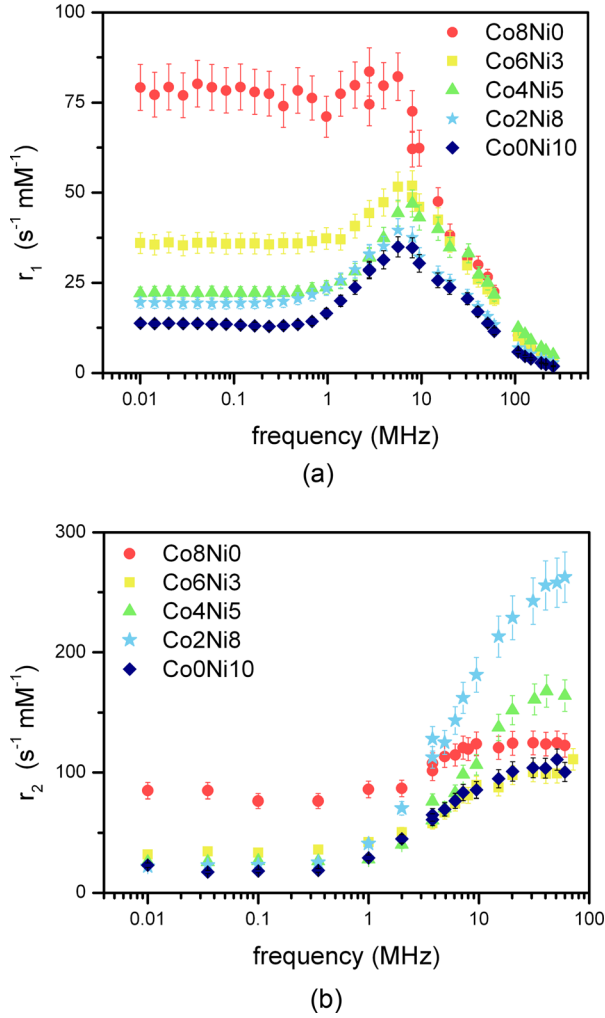


FIG. 8. Longitudinal (a) and transverse (b) relaxivity profiles of Co-Ni-ferrites. The evolution of the low field behaviour of r_1 from stoichiometric Co-ferrite (Co8Ni0, in red) to stoichiometric Ni-ferrite (Co0Ni10, in dark blue) is easy to follow.

1 MHz), which is a typical feature of low magnetic anisotropy barrier. Increasing the amount of cobalt, at first the low field dispersion disappears, then the maximum becomes less and less evident. In the limit case of stoichiometric Co-ferrite (Co8Ni0), r_1 appears flat at low frequencies, i.e., $\nu < 8$ MHz, and then drops rapidly at higher frequencies. Indeed, in this case, the high magnetic anisotropy suppresses the reorientation of the nanoparticles magnetic moment μ_{SP} (Néel relaxation) even at low fields, increasing the relaxation rate.

A similar scaling effect cannot be seen for the transverse relaxivity (r_2) (Fig. 8(b)). However, the complete profile, acquired over the range 10 kHz–60 MHz, qualitatively reproduces the theoretical one, predicted by Roch *et al.* in Ref. 18. The transverse relaxivity values allow the evaluation of the efficiency as contrast agents for magnetic resonance imaging, because the higher the r_2 , the better the image contrast. Since the final goal is the clinical application of such nanostructures, we focused our attention on the values of the transverse relaxivity assumed in correspondence of the magnetic field commonly used by MRI scanner, i.e., $H = 0.5$ and 1.5 T, corresponding to $\nu = 21$ and 64 MHz for the proton. All the

samples display a value of r_2 in the range 85 – 125 $s^{-1}mM^{-1}$ for both frequencies, except Co2Ni8, which exhibits a higher value, being $r_2 = 262$ $s^{-1}mM^{-1}$. In all cases, these values are comparable or higher to the ones of Endorem, a former clinical contrast agent often taken as reference compounds, which has $r_2 \sim 90$ $s^{-1}mM^{-1}$ at clinical frequencies.

VII. DATA ANALYSIS

Roch *et al.* proposed in Ref. 18 an heuristic model for the relaxation rates $1/T_1$ and $1/T_2$, which is a linear combination of the relaxation rates in the limit of large anisotropy ($E_b \rightarrow \infty$) and zero anisotropy ($E_b = 0$)

$$\frac{1}{T_1} = \frac{32\pi}{135000} \mu_{SP}^2 \gamma_I^2 \left(\frac{N_{AC}}{D r_d} \right) \left\{ 7P \frac{L(x)}{x} J^F(\omega_S) + \left[7(1-P) \frac{L(x)}{x} + 3 \left(1 - L^2(x) - \frac{2L(x)}{x} \right) \right] \times J^F(\omega_I) + 3L^2(x) J^A \left(\sqrt{2\omega_I \tau_D} \right) \right\}, \quad (6)$$

$$\frac{1}{T_2} = \frac{16\pi}{135000} \mu_{SP}^2 \gamma_I^2 \left(\frac{N_{AC}}{D r_d} \right) \left\{ 13P \frac{L(x)}{x} J^F(\omega_S) + 7(1-P) \frac{L(x)}{x} J^F(\omega_I) + 6(1-P) \frac{L(x)}{x} J^F(0) + \left[1 - L^2(x) - \frac{2L(x)}{x} \right] \cdot \left[3J^F(\omega_I) + 4J^F(0) \right] + L^2(x) \left[3J^A \left(\sqrt{2\omega_I \tau_D} \right) + 4J^A(0) \right] \right\}. \quad (7)$$

The factor P can vary in the range $0 \leq P \leq 1$ and represents the coefficient of the linear combination: in particular, for $P = 0$ one obtains the infinite anisotropy term, while for $P = 1$ the zero anisotropy one. $L(x)$ is the Langevin function $L(x) = \coth(x) - 1/x$ and describes the particle magnetization as a function of the applied magnetic field. Its argument is $x = \mu_0 \mu_{SP} H / k_B T$. This function is used to properly weigh the low field contribution, described by J^F , the Freed density function, and the high field contribution, described by the Ayant density function J^A . In particular, J^F and J^A are⁴⁸

$$J^F(\omega) = \text{Re} \left\{ \frac{1 + \frac{\Omega^{1/2}}{4}}{1 + \Omega^{1/2} + \frac{4\Omega}{9} + \frac{\Omega^{3/2}}{9}} \right\}, \quad (8)$$

where $\Omega = (i\omega + 1/\tau_N) \cdot \tau_D$, and

$$J^A(z) = \frac{1 + \frac{5 \cdot z}{8} + \frac{z^2}{8}}{1 + z + \frac{z^2}{2} + \frac{z^3}{6} + \frac{4 \cdot z^4}{81} + \frac{z^5}{81} + \frac{z^6}{648}}, \quad (9)$$

where the argument is $z = \sqrt{2\omega_I \tau_D}$, ω_I being the nuclear Larmor frequency.

The fit was performed considering four parameters: (i) the magnetic core size r_{NMR} , which is necessary to calculate μ_{SP} and was constrained within the variability range of d_{TEM} (Table I); (ii) the Néel relaxation time τ_N without variability

constraints; (iii) the factor P , which due to the large magnetic anisotropy of our samples, was set to $P=0$ in all cases, except for the Co0Ni10, for which was chosen $P=0.15$ to properly fit the low field profile; and (iv) the minimum approach distance r_d , i.e., the distance between the center of the ferrite nanoparticle and the closest diffusing water molecule. This parameter is crucial in determining the characteristic diffusion time τ_D of the water relatively to the nanoparticle, that is expressed as $\tau_D = r_d^2/D$, where $D = 2.3 \times 10^{-9} \text{ m}^2/\text{s}$ is the water self diffusion coefficient. Since the coating has a fundamental role in r_d estimation, the variability range was assessed by AFM results, taking the height value as minimum and the width as maximum.

The longitudinal relaxivity model is nowadays well-established and successfully used in r_1 data analysis for particles having a core diameter $d \leq 20 \text{ nm}$. On the contrary, the transverse relaxometry measurements are not so commonly reported in the literature, and complete experimental relaxometry profiles are missing. Indeed, r_2 is generally measured only at specific fields, which usually match the ones of the clinical MRI machines (typically 0.5, 1.5, and 3 T), in order to verify the efficiency of the analyzed compound as contrast agent. For these reasons, the Roch model has not been completely verified yet.

Since both the longitudinal and the transverse relaxivities were deduced within the same theoretical framework, the r_1 and r_2 curves are strongly connected. In particular, the same set of parameters that is used to fit the longitudinal relaxometry data should fit (within the experimental error) the transverse relaxivity ones. However, a simultaneous fit of both the curves was not successful. As a consequence, first we fitted the r_1 data, being this procedure well-known and reliable, and then we used the obtained parameters to

simulate the transverse relaxivity curve with Eq. (7) in order to compare it to the experimental data.

The results of this procedure are shown in Fig. 9, while the numerical values of the parameters obtained from the r_1 fit (and then used in r_2 calculation) are summarized in Table IV. The quality of the r_1 fit is rather good, and the curves reproduce the experimental relaxometry profiles, both when the maximum is well-defined (Co0Ni10) and when there is the typical high anisotropy plateau (Co8Ni0). On the contrary, the r_2 calculated profiles are far from the experimental data: as can be seen at a first glance, although for $\nu < 1 \text{ MHz}$ the condition $r_1 = r_2$ requested by the theory is experimentally verified, the r_2 theoretical predictions do not reproduce the experimental data in the high frequency region (i.e., $\nu > 1 - 10 \text{ MHz}$). In particular, the calculated r_2 value is lower than the experimental one. This discrepancy could be an indication of the fact that some relaxation mechanisms which introduce a transverse dephasing are neglected in the theoretical model. A possible explanation could be related to the existence of a sort of first coordination sphere in the surroundings of the magnetic particle, where the waters' protons stay (on average) for a time longer than τ_D , as usually happens for Gd-compounds.^{49,50}

The order of magnitude of the Néel relaxation time obtained by NMR measurements, τ_N^{NMR} , is in the typical range for superparamagnetic systems' reversal time, i.e., $10^{-10} - 10^{-7} \text{ s}$. In Fig. 10, τ_N^{NMR} is compared to τ_N^{AC} obtained from AC susceptibility measurements using the experimental parameters of Table III in Eq. (4) and considering $T = 300 \text{ K}$. For all the samples, τ_N^{NMR} results lower than τ_N^{AC} . Part of this difference has to be ascribed to the different intensity of the interparticle interactions in the two cases.⁵¹ Indeed, the powder samples (where NPs are in close contact) were used for

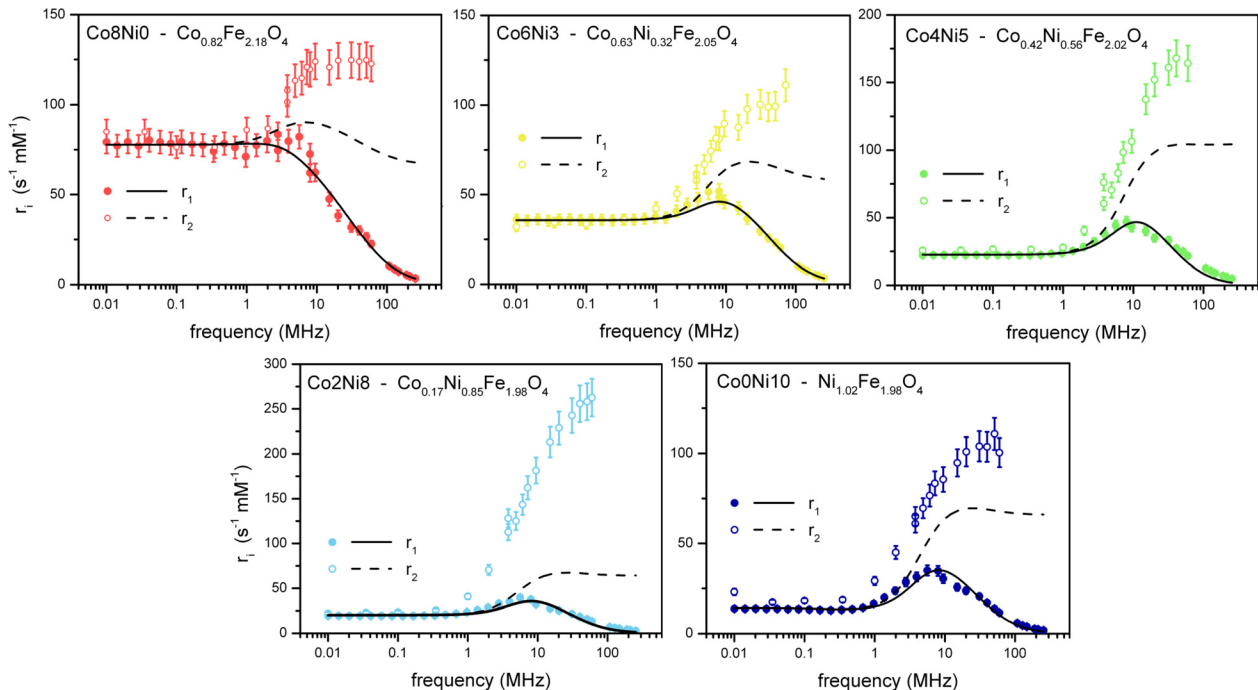


FIG. 9. Best-fits of the longitudinal relaxivity profiles r_1 and predictions of the transverse relaxivity. The heuristic version of the Roch model,¹⁸ i.e., Eqs. (6) and (7), was used.

TABLE IV. Best-fit parameters r_{NMR} , r_d , and τ_N^{NMR} obtained applying Eq. (6) to r_1 profiles. The standard error given by the algorithm is reported in brackets. Numerical values of M_S (used to calculate μ_{SP} , r_{TEM} , and r_{AFM} previously discussed and used as input data for fitting procedure (see text for details) are here reported for clarity. The same values of r_{NMR} , r_d , τ_N^{NMR} , and P were introduced in Eq. (7) to predict the transverse relaxivity r_2 .

Sample	M_S (A m ² /kg)	r_{TEM} (nm)	r_{AFM} (nm)	NMR fitting parameters			P
				r_{NMR} (nm)	r_d (nm)	τ_N^{NMR} (s)	
Co8Ni0	87	3.7 ± 0.7	4.0 – 6.9	4.3(1.7)	5.0(0.1)	4.7(1.2) × 10 ⁻⁸	0
Co6Ni3	62	3.5 ± 0.6	4.0 – 6.9	4.0(0.2)	4.8(0.1)	4.9(0.3) × 10 ⁻⁹	0
Co4Ni6	47	3.3 ± 0.5	4.3 – 7.3	4.0(0.2)	6.9(0.4)	1.7(0.2) × 10 ⁻⁹	0
Co2Ni8	54	3.5 ± 0.6	4.4 – 7.5	4.1(0.1)	6.8(0.4)	2.9(0.3) × 10 ⁻⁹	0
Co0Ni10	49	3.7 ± 0.8	4.2 – 6.9	4.5(0.2)	6.9(0.4)	1.7(0.2) × 10 ⁻⁹	0.15

AC susceptibility measurements, while the NMR relaxometry measurements were performed on water dispersions, where dipolar interactions among the particles are weaker than in powders. Furthermore, it should be noticed that AC susceptibility is a bulk technique that provides results averaged over the whole sample volume, while NMR is a local probe and so it has a different sensitivity to the effects of long-range dipolar interparticle interactions in solution:⁵² the diffusional motions of the particles generally average the short-range interaction to zero and the long-range interactions to a negligible amount.⁵³ However, even if a great discrepancy is present for Co0Ni10, the general behaviour of the reversal time as a function of the doping is the same for both techniques. A minimum of the Néel relaxation time is observed when the amount of both Ni and Co is ~ 0.5 . This behaviour is difficult to interpret with simple arguments referring to the evolution of the magnetic properties, and it will deserve more attention in future investigations.

VIII. CONCLUSION

The effect of metal doping in iron oxide nanoparticles was systematically studied using a series of five $\text{Co}_x\text{Ni}_y\text{Fe}_{3-x-y}\text{O}_4$ samples having similar size and following a step by step doping, going from stoichiometric Co-ferrite to stoichiometric Ni-ferrite. The mean diameter of the magnetic core was for all

the samples 7 nm with a narrow size distribution, as observed by TEM images. Besides this standard technique, the tapping mode AFM was used to study the particle morphology and revealed itself as a useful tool for the characterization of coated NPs, being sensitive to both the core and the coating. Combining topography and phase measurements, a coating thickness of 2 nm was evaluated.

The magnetic properties were investigated by means of DC and AC susceptibility measurements. In particular, the effective magnetic anisotropy was evaluated by using the anisotropy barrier value roughly estimated from the fit of the low field ZFC curves (approximating the systems as a collection of non-interacting nanoparticles). A qualitative trend of the magnetic anisotropy as a function of the doping was disclosed, singled out to be proportional to the amount of cobalt. On the contrary, the nickel doping has an opposite effect, as revealed from the fact that the stoichiometric Ni-ferrite exhibits an anisotropy even lower than the undoped ferrite taken as reference. The AC measurements allowed us to explore the Néel relaxation of the particles magnetization by evaluating the characteristic relaxation time τ_N , which ranges between 10⁻⁹ s and 10⁻⁷ s at 300 K. Furthermore, τ_N shows a trend having a minimum in correspondence to doping Co ~ 0.5 and Ni ~ 0.5 .

The longitudinal (r_1) and transverse (r_2) relaxometry measurements were performed in water suspensions. The anisotropy doping dependence is confirmed by the r_1 profiles as a function of doping. The well-known Roch model was successfully used to fit the r_1 data, taking into account the morphological results from TEM and AFM as variability constrains for the magnetic core and the coating layer sizes. The qualitative behaviour of the Néel relaxation time estimated by NMR is consistent with the one obtained from AC susceptibility. The r_2 expression resulting from the Roch's model was tested for the first time over a wide range of frequencies using the best-fit parameters obtained for r_1 profiles. The agreement with the experimental data is very poor, especially in the high frequency region. Being the measured r_2 values always higher than the predicted ones, it is reasonable to assume the existence of a further relaxation mechanism neglected by the theory and possibly related to the presence of an inner sphere around the nanoparticle, where the protons strongly interact with the magnetic moment of the particle.

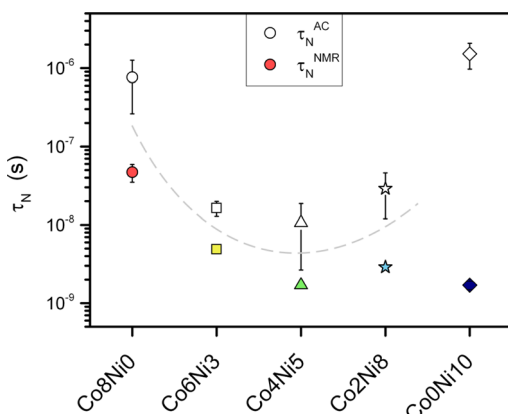


FIG. 10. Néel relaxation time τ_N evaluated with two different techniques: AC susceptibility (open symbols) and NMR relaxometry (solid symbols). The dashed line is for the eyes.

ACKNOWLEDGMENTS

The research was coordinated under the Project FIRB RINAME No. RBAP114AMK. The Fondazione Cariplo, through Project Nos. 2013-0752 “BaTMAN,” 2010-0612, and 2012-0872, and the Fondazione Banca del Monte di Lombardia are also acknowledged.

- ¹L. Néel, *Rev. Mod. Phys.* **25**, 293 (1953).
- ²W. F. Brown, *Phys. Rev.* **130**, 1677 (1963).
- ³L. Bordonali, Y. Furukawa, M. Kraken, F. J. Litterst, C. Sangregorio, M. F. Casula, and A. Lascialfari, *Phys. Rev. B* **85**, 174426 (2012).
- ⁴M. Colombo, S. Carregal-Romero, M. F. Casula, L. Gutiérrez, M. P. Morales, I. B. Böhm, J. T. Heverhagen, D. Prospero, and W. J. Parak, *Chem. Soc. Rev.* **41**, 4306 (2012).
- ⁵Q. Pankhurst, J. Connolly, and S. Jones, *J. Phys. D: Appl. Phys.* **36**, R167 (2003).
- ⁶Q. Pankhurst, N. Thanh, S. Jones, and J. Dobson, *J. Phys. D: Appl. Phys.* **42**, 224001 (2009).
- ⁷M. F. Casula, P. Floris, C. Innocenti, A. Lascialfari, M. Marinone, M. Corti, R. A. Sperling, W. J. Parak, and C. Sangregorio, *Chem. Mater.* **22**, 1739 (2010).
- ⁸P. Arosio, J. Thévenot, T. Orlando, F. Orsini, M. Corti, M. Mariani, L. Bordonali, C. Innocenti, C. Sangregorio, H. Oliveira, S. Lecommandoux, A. Lascialfari, and O. Sandre, *J. Mater. Chem. B* **1**, 5317 (2013).
- ⁹F. Scherer, M. Anton, U. Schillinger, J. Henke, C. Bergemann, A. Kruger, B. Gansbacher, and C. Plank, *Gene Ther.* **9**, 102 (2002).
- ¹⁰A. Jordan, R. Scholz, K. Maier-Hauff, M. Johannsen, P. Wust, J. Nadobny, H. Shirra, H. Schmidt, S. Deger, S. Loening, W. Lanksch, and R. Felix, *J. Magn. Magn. Mater.* **225**, 118 (2001); S. Dutz and R. Hergt, *Nanotechnology* **25**, 452001 (2014).
- ¹¹R. Kappiyoor, M. Liangruksa, R. Ganguly, and I. K. Puri, *J. Appl. Phys.* **108**, 094702 (2010).
- ¹²E. Kita, S. Hashimoto, T. Kayano, M. Minagawa, H. Yanagihara, M. Kishimoto, K. Yamada, T. Oda, N. Ohkohchi, T. Takagi, T. Kanamori, Y. Ikehata, and I. Nagano, *J. Appl. Phys.* **107**, 09B321 (2010).
- ¹³P. Drake, H.-J. Cho, P.-S. Shih, C.-H. Kao, K.-F. Lee, C.-H. Kuo, X.-Z. Lin, and Y.-J. Lin, *J. Mater. Chem.* **17**, 4914 (2007).
- ¹⁴Y. Zhang, G. K. Das, R. Xu, and T. T. Yang Tan, *J. Mater. Chem.* **19**, 3696 (2009).
- ¹⁵J. T. Jang, H. Nah, J. H. Lee, S. H. Moon, M. G. Kim, and J. Cheon, *Angew. Chem.* **121**, 1260 (2009).
- ¹⁶E. Fantechi, G. Campo, D. Carta, A. Corrias, C. de Julian Fernandez, D. Gatteschi, C. Innocenti, F. Pineider, F. Ruggi, and C. Sangregorio, *J. Phys. Chem. C* **116**, 8261 (2012).
- ¹⁷J. Elizalde Galindo, A. Adair, C. Botez, V. Corral Flores, D. Bueno Baques, L. Fuentes Cobas, and J. Matutes-Aguino, *Appl. Phys. A* **87**, 743 (2007).
- ¹⁸A. Roch, R. N. Muller, and P. Gillis, *J. Chem. Phys.* **110**, 5403 (1999).
- ¹⁹R. Kimmich and E. Anoardo, *Prog. Nucl. Magn. Reson. Spectrosc.* **44**, 257 (2004).
- ²⁰G. Ferrante and S. Sykora, *Adv. Inorg. Chem.* **57**, 405 (2004).
- ²¹R. Yanes, O. Chubykalo-Fesenko, H. Kachkachi, D. A. Garanin, R. Evans, and R. W. Chantrell, *Phys. Rev. B* **76**, 064416 (2007).
- ²²R. Valenzuela, *Magnetic Ceramics* (Cambridge University Press, Cambridge, 1984).
- ²³J. Wang, *Mater. Sci. Eng., B* **127**, 81 (2006).
- ²⁴G. Muscas, N. Yaacoub, G. Concas, F. Sayed, R. Sayed Hassan, J. M. Greneche, C. Cannas, A. Musinu, V. Foglietti, S. Casciardi, C. Sangregorio, and D. Peddis, *Nanoscale* **7**, 13576 (2015).
- ²⁵E. Umot, F. Pineider, P. Arosio, C. Sangregorio, M. Corti, F. Tabak, A. Lascialfari, and P. Ghigna, *J. Magn. Magn. Mater.* **324**, 2373 (2012).
- ²⁶M. Hansen and S. Mørup, *J. Magn. Magn. Mater.* **203**, 214 (1999).
- ²⁷F. Tournus and E. Bonet, *J. Magn. Magn. Mater.* **323**, 1109 (2011).
- ²⁸F. Tournus and A. Tamion, *J. Magn. Magn. Mater.* **323**, 1118 (2011).
- ²⁹S. Morup and E. Tronc, *Phys. Rev. Lett.* **72**, 3278 (1994).
- ³⁰P. Allia, M. Coisson, P. Tiberto, F. Vinai, M. Knobel, M. A. Novak, and W. C. Nunes, *Phys. Rev. B* **64**, 144420 (2001).
- ³¹X. Batlle and A. Labarta, *J. Phys. D: Appl. Phys.* **35**, R15 (2002).
- ³²A. M. Pereira, C. Pereira, A. S. Silva, D. S. Schmol, C. Freire, J.-M. Grenche, and J. P. Arajo, *J. Appl. Phys.* **109**, 114319 (2011).
- ³³D. Peddis, F. Orru, A. Ardu, C. Cannas, A. Musinu, and G. Piccaluga, *Chem. Mater.* **24**, 1062 (2012).
- ³⁴A. Hillion, M. Pauly, A. Tamion, F. Tournus, M. Hillenkamp, B. P. Pichon, S. Begin-Colin, and V. Dupuis, *J. Appl. Phys.* **112**, 123902 (2012).
- ³⁵A. Hillion, A. Tamion, F. Tournus, O. Gaier, E. Bonet, C. Albin, and V. Dupuis, *Phys. Rev. B* **88**, 094419 (2013).
- ³⁶F. Tournus, A. Hillion, A. Tamion, and V. Dupuis, *Phys. Rev. B* **87**, 174404 (2013).
- ³⁷P. Allia, G. Barrera, P. Tiberto, T. Nardi, Y. Leterrier, and M. Sangermano, *J. Appl. Phys.* **116**, 113903 (2014).
- ³⁸C. Moya, Ó. Iglesias, X. Batlle, and A. Labarta, *J. Phys. Chem. C* **119**, 24142 (2015).
- ³⁹B. Aslibeiki, P. Kameli, and H. Salamati, *J. Appl. Phys.* **119**, 063901 (2016).
- ⁴⁰M. Okuda, J. C. Eloi, A. Sarua, S. E. Ward Jones, and W. Schwarzacher, *J. Appl. Phys.* **111**, 07B519 (2012).
- ⁴¹O. Iglesias and A. Labarta, *Phys. Rev. B* **70**, 144401 (2004).
- ⁴²L. E. Wenger and J. A. Mydosh, *Phys. Rev. B* **29**, 4156 (1984).
- ⁴³G. F. Goya and M. P. Morales, *J. Metastable Nanocryst. Mater.* **20–21**, 673 (2004).
- ⁴⁴W. Luo, S. R. Nagel, T. Rosenbaum, and R. Rosensweig, *Phys. Rev. Lett.* **67**, 2721 (1991).
- ⁴⁵S. Mørup, M. F. Hansen, and C. Frandsen, *Beilstein J. Nanotechnol.* **1**, 182 (2010).
- ⁴⁶E. Tronc, P. Prene, J. P. Jolivet, F. D’Orazio, F. Lucari, D. Fiorani, M. Godinho, R. Cherkaoui, M. Noguez, and J. L. Dormann, *Hyperfine Interact.* **95**, 129 (1995).
- ⁴⁷J. L. Dormann, D. Fiorani, and E. Tronc, in *Advances in Chemical Physics*, Vol. 98, edited by I. Prigogine and S. A. Rice (John Wiley & Sons, Inc., 1997), Chap. 4, pp. 283–494.
- ⁴⁸J. Freed, *J. Chem. Phys.* **68**, 4034 (1978).
- ⁴⁹P. Gillis, A. Roch, and R. A. Brooks, *J. Magn. Reson.* **137**, 402 (1999).
- ⁵⁰S. Laurent, L. V. Elst, A. Roch, and R. N. Muller, in *NMR-MRI, μ SR and Mössbauer Spectroscopies in Molecular Magnets*, edited by P. Carretta and A. Lascialfari (Springer, 2007), pp. 71–87.
- ⁵¹C. Djurberg, P. Svedlindh, P. Nordblad, M. Hansen, F. Bødker, and S. Mørup, *Phys. Rev. Lett.* **79**, 5154 (1997).
- ⁵²L. Bordonali, T. Kalaivani, K. Sabareesh, C. Innocenti, E. Fantechi, C. Sangregorio, M. F. Casula, L. Lartigue, J. Larionova, Y. Guari, M. Corti, P. Arosio, and A. Lascialfari, *J. Phys.: Condens. Matter* **25**, 066008 (2013).
- ⁵³M. H. Levitt, *Spin Dynamics: Basis of Nuclear Magnetic Resonance* (John Wiley & Sons, Chichester, 2008).